

ACCEPTED MANUSCRIPT • OPEN ACCESS

# Model-Driven Analysis of Ion Transport for the Design of Efficient Membrane-Based Electrochemical CO<sub>2</sub> Capture

To cite this article before publication: Marco Colin Martinez *et al* 2026 *J. Electrochem. Soc.* in press <https://doi.org/10.1149/1945-7111/ae55d3>

## Manuscript version: Accepted Manuscript

Accepted Manuscript is “the version of the article accepted for publication including all changes made as a result of the peer review process, and which may also include the addition to the article by IOP Publishing of a header, an article ID, a cover sheet and/or an ‘Accepted Manuscript’ watermark, but excluding any other editing, typesetting or other changes made by IOP Publishing and/or its licensors”

This Accepted Manuscript is © 2026 The Author(s). Published on behalf of The Electrochemical Society by IOP Publishing Limited.

As the Version of Record of this article is going to be/has been published on a gold open access basis under a CC 4.0 licence, this Accepted Manuscript is available for reuse under the applicable CC licence immediately.

Everyone is permitted to use all or part of the original content in this article, provided that they adhere to all the terms of the applicable licence referred to in the article – either <https://creativecommons.org/licenses/by/4.0/> or <https://creativecommons.org/licenses/by-nc-nd/4.0/>

Although reasonable endeavours have been taken to obtain all necessary permissions from third parties to include their copyrighted content within this article, their full citation and copyright line may not be present in this Accepted Manuscript version. Before using any content from this article, please refer to the Version of Record on IOPscience once published for full citation and copyright details, as permissions may be required. All third party content is fully copyright protected and is not published on a gold open access basis under a CC licence, unless that is specifically stated in the figure caption in the Version of Record.

View the [article online](#) for updates and enhancements.

---

**Model-Driven Analysis of Ion Transport for the Design of Efficient Membrane-Based Electrochemical CO<sub>2</sub> Capture**

Journal:	<i>Journal of The Electrochemical Society</i>
Manuscript ID	JES-115855.R1
Manuscript Type:	Research Paper
Date Submitted by the Author:	01-Mar-2026
Complete List of Authors:	Colin Martinez, Marco; University of Delaware, Setzler, Brian; University of Delaware, Chemical and Biomolecular Engineering Yan, Yushan; University of Delaware, Chemical and Biomolecular Engineering
Keywords:	Design, Electrochemical Engineering, Membranes and Separators, Electrode Kinetics

SCHOLARONE™  
Manuscripts

# Model-Driven Analysis of Ion Transport for the Design of Efficient Membrane-Based Electrochemical CO<sub>2</sub> Capture

Marco Colin Martinez, Brian P. Setzler, and Yushan Yan<sup>\*,z</sup>

Center for Clean Hydrogen &

Department of Chemical and Biomolecular Engineering,

University of Delaware, Newark, Delaware 19716, USA

<sup>\*</sup>Electrochemical Society Fellow.

<sup>z</sup>E-mail: [yanys@udel.edu](mailto:yanys@udel.edu)

## Abstract

Reducing energy consumption is essential for electrochemical direct air capture (DAC) of CO<sub>2</sub> to reach the Department of Energy (DOE) cost target of \$100/tonCO<sub>2</sub>. However, membrane-based electrochemical DAC systems typically exhibit electron efficiencies below 40% (mol CO<sub>2</sub>/mol e<sup>-</sup>), in part due to an incomplete understanding of ion transport. To address this limitation, we developed a one-dimensional electrochemical model for hydrogen-powered hydroxide exchange membrane carbon capture (H<sub>2</sub>-HEMCC) systems. Validated against experiments, the model revealed two dominant inefficiencies: carbonate diffusion losses and hydroxide diffusion losses at low and high CO<sub>2</sub> flux, respectively. Guided by these insights, we experimentally show improved efficiency at low flux through higher membrane resistance, achieved via thermal degradation of quaternary ammonium sites. To overcome high-flux losses, we introduced a thick interlayer between the membrane and cathode, which suppresses hydroxide diffusion losses that dominate at high flux, where capital costs are lower. This strategy raised experimental peak electron efficiency from 38.7% to 63.8%, the highest reported for any membrane-based DAC system. It translates to \$23/tonCO<sub>2</sub> in energy savings—nearly one quarter of the DOE target. Model projections further indicate that employing a carbonate-rejecting ionomer could elevate efficiencies beyond 75%, providing a new pathway for high-performance, low-energy electrochemical DAC systems.

## Introduction

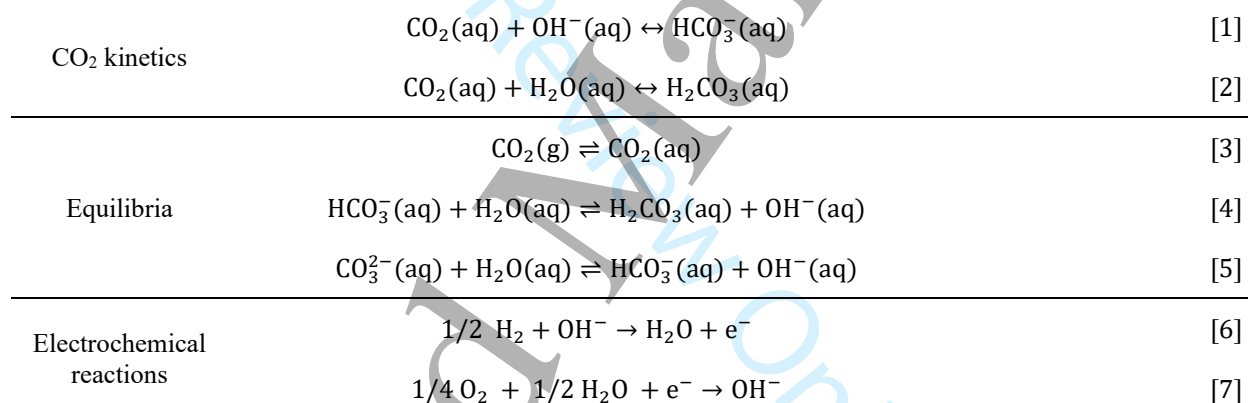
Billions of tons of CO<sub>2</sub> annual emissions are driving global warming, posing a serious threat to climate stability and human well-being.<sup>1</sup> Achieving global net-zero CO<sub>2</sub> emissions by 2050 is essential to limit warming to 1.5 °C above pre-industrial levels, as modeled by the Intergovernmental Panel on Climate Change (IPCC) and International Energy Agency (IEA), to prevent the most severe climate impacts.<sup>1,2</sup> In 2024, the Berkeley Earth Global Temperature Report shows that the annual average rise surpassed 1.62 °C, highlighting that we are already behind schedule and must rapidly accelerate emission reductions to remain near the 1.5 °C target.<sup>3</sup> Although transitioning all CO<sub>2</sub>-emitting technologies to renewable energy is necessary, it alone cannot achieve net-zero emissions because some sectors,<sup>4</sup> such as iron and steel, heavy-duty trucking, shipping, and aviation, are difficult to fully decarbonize, and significant historical CO<sub>2</sub> remains in the atmosphere.<sup>5</sup>

Addressing this residual CO<sub>2</sub> will require direct air capture (DAC), the only scalable technology capable of removing CO<sub>2</sub> directly from ambient air. To reach global net-zero CO<sub>2</sub> emissions, gigaton-scale direct air capture will be necessary by 2050, according to the IEA.<sup>6</sup> Consequently, the Department of Energy (DOE) has set a target of \$100/tonCO<sub>2</sub> to make this scale reachable. Among DAC technologies, the most advanced are liquid and solid sorbents, with net removed costs ranging from \$126 to 780/tonCO<sub>2</sub> and \$124 to 407/tonCO<sub>2</sub>, respectively.<sup>7</sup> Despite these advances, these technologies rely on large temperature regeneration requirements, resulting in significant thermal energy demands.<sup>7</sup>

Electrochemical direct air capture (DAC) of CO<sub>2</sub>, on the other hand, operates at low temperatures, does not need separate regeneration equipment, and is powered by renewable electricity or hydrogen.<sup>8-13</sup> To reach commercialization, however, the selected technology must be economically viable. The desired performance metrics for lower cost electrochemical capture are low device energy consumption, high CO<sub>2</sub> flux, and high CO<sub>2</sub> removal per pass.

This work focuses on a hydrogen-powered hydroxide exchange membrane carbon capture (H<sub>2</sub>-HEMCC) system, where H<sub>2</sub> serves as the sole energy source and thus its energy consumption only depends on electron efficiency. The H<sub>2</sub>-HEMCC operates with a finite open-circuit voltage that is drawn down to generate current and drive CO<sub>2</sub> capture. In this study, unused cell voltage is not recovered, and the system energy is therefore evaluated exclusively in terms of electron efficiency. As seen from Fig. 1a, high electron efficiencies are critical for the commercialization of the H<sub>2</sub>-HEMCC. Electron efficiencies under 23% lead to hydrogen cost exceeding the DOE target of \$100/tonCO<sub>2</sub>, even before other cost contributions are considered. Understanding the processes and variables that affect electron efficiency requires a closer look at the device architecture and chemistry.

The H<sub>2</sub>-HEMCC architecture is shown in Fig. 1b, and it concentrates CO<sub>2</sub> from the cathode inlet to the anode outlet. At the cathode, 400 ppm CO<sub>2</sub> in air enters and exits as a CO<sub>2</sub>-lean air stream. At the anode, a small stream of pure hydrogen enters, and the outlet stream contains a highly concentrated CO<sub>2</sub> stream (>70% mol/mol), where the purity depends on the electron efficiency and hydrogen consumption. The nickel mesh is employed to facilitate CO<sub>2</sub> transport to the cathode, while the gas diffusion layer (GDL) serves as a diffusion medium that distributes hydrogen to the anode. As discussed in Matz et al.,<sup>9</sup> the HEMCC operates based on aqueous CO<sub>2</sub> kinetics (Eq. 1-2) and equilibria (Eq. 3-5), where the pH is driven by the electrochemical reactions occurring at the half-cells (Eq. 6-7).



The oxygen reduction reaction (ORR) produces a high-pH environment at the cathode, while the hydrogen oxidation reaction (HOR) generates a lower-pH environment at the anode. The ORR produces hydroxides that react with CO<sub>2</sub> (Eq. 1) contained within the cathode and interlayer, forming bicarbonates that equilibrate to carbonates (Eq. 5). These carbonates are transported from the cathode to the anode. At the anode, carbonates accumulate and HOR consumes hydroxides, resulting in a decreased pH, which shifts the ionic equilibrium to bicarbonate. This bicarbonate forms carbonic acid, which rapidly decomposes to release pure CO<sub>2</sub> at the anode outlet (Eq. 2).

Because electron efficiency has a substantial influence on DAC cost, it is critical to identify the key parameters that improve performance. Electron efficiency is defined as the ratio of CO<sub>2</sub> flux to electron flux and can be related to ion transport through Faraday's law and a steady-state CO<sub>2</sub> balance in the membrane:

$$\eta_e = \frac{N_{\text{CO}_2}}{I/F} = \frac{N_C + N_B}{2N_C + N_B + N_H} \quad [8]$$

where  $\eta_e$  is electron efficiency,  $I$  is current density,  $F$  is Faraday's constant.  $N_C$ ,  $N_H$ , and  $N_B$  are the fluxes of carbonate, hydroxide, and bicarbonate ions, respectively. As seen from Eq. 8 and Fig. 1a, electron efficiency is maximally bound by bicarbonate transport, whereas pure carbonate transport is limited to a maximum electron efficiency of 50%, owing to its divalent charge.

Achieving high electron efficiency remains a major challenge in membrane-based electrochemical direct air capture systems, as values typically fall below 40%. This limitation in part arises from an incomplete understanding of the ion transport mechanisms that govern system performance. This lack of mechanistic insight restricts the ability to design materials and architectures to achieve competitive performance. Consequently, modeling transport mechanisms is essential to drive the system to lower energy costs.

Prior modeling of CO<sub>2</sub> effects in hydroxide exchange membrane systems has focused almost exclusively on hydroxide-exchange membrane fuel cells (HEMFCs), where CO<sub>2</sub> is a source of performance loss. Early work by Siroma et al. introduced a 1D Nernst-Planck model showing self-purging of carbonate at higher current density, with (bi)carbonate accumulating at the anode and thicker membranes retaining more carbonate.<sup>14</sup> Grew et al. developed a temperature-dependent equilibrium model demonstrating that CO<sub>2</sub> severely reduces ionic conductivity with stronger effects at lower temperatures.<sup>15</sup> Subsequent models added water management and electrochemistry. Shiao et al., for instance, used a 2D model to reveal that CO<sub>2</sub>-induced pH gradients were mitigated by higher current.<sup>16</sup> Wrubel et al. and Krewer et al. confirmed via transient 1D models that high current densities reduce carbonate site fraction and drive self-purging.<sup>17,18</sup> Gerhardt et al. employed a 1+2D along-the-channel framework—a 2D computational model of an HEMFC cell coupled with a 1D down-channel stepping algorithm—further corroborating previous results showing (bi)carbonate buildup at the anode, and developed an overpotential loss breakdown including CO<sub>2</sub> effects.<sup>19</sup> Only Matz et al. explicitly targeted CO<sub>2</sub> removal developing a simplified, 1D analytical model, and improved CO<sub>2</sub> capture through mass transport resistance minimization.<sup>9</sup> That work, however, focused the modeling for a HEMFC pretreatment device rather than a standalone carbon capture device.

Collectively, these works reveal the insights that lower current density and low temperatures increase (bi)-carbonates site fraction. Paradoxically, they show that higher membrane resistance promotes (bi)-carbonate accumulation, an undesirable effect in fuel cells but possibly advantageous for carbon capture. Moreover, all models focus on high-currents to show mitigation of CO<sub>2</sub> poisoning rather than low-current (<20 mA/cm<sup>2</sup>) operation.

Building on this knowledge of CO<sub>2</sub> in HEMFCs, we develop an experimentally validated one-dimensional multi-layer model to elucidate transport behavior in the H<sub>2</sub>-HEMCC system. We also introduce a diagnostic framework for electron efficiency that quantitatively identifies efficiency-loss mechanisms and supports hypothesis generation for improving performance. Through this analysis, we confirm that increasing membrane resistance enhances electron efficiency by reducing carbonate diffusion losses; however, this improvement is limited to low flux values. To address this limitation, a thick interlayer was implemented, which further improves performance by shifting the peak electron efficiency to higher fluxes, where capital cost is lower. Experimentally (Fig. 1a), we achieve a peak electron efficiency of 63.8% relative to the baseline 38.7% resulting in savings roughly equal to a quarter of the DOE target (\$23/tonCO<sub>2</sub>). For higher electron efficiencies, we explored a new pathway through modeling involving transport rejection of carbonate. By suppressing carbonate conductivity, we demonstrate that electron efficiencies can surpass 75% as ion transport approaches pure bicarbonate conduction.

## Experimental Methods

### *Membrane electrode assembly (MEA) preparation*

Membrane electrode assemblies (MEAs) were prepared using 40um PiperIon® membranes (Versogen) as the hydroxide exchange membrane with an active area of 25 cm<sup>2</sup>. The anode and cathode catalysts consisted of 40 wt% Pt/C (Vulcan XC-72R, Fuel Cell Store), and the hydroxide exchange ionomer (HEI) was a 5 wt% PiperIon® solution (Versogen). A carbon interlayer composed of Vulcan XC-72 (Fuel Cell Store) and HEI was used between the cathode catalyst layer and the membrane. Catalyst inks were prepared by dispersing the appropriate amounts (Table I) of Pt/C, carbon, and ionomer in an isopropanol–water mixture, followed by sonication in an ice bath for 1 h. The inks were air-sprayed directly onto the membrane using an Iwata hand spray gun, sequentially depositing the interlayer, cathode, and anode layers to form the MEA.

### *Cell assembly*

The MEA was assembled in single-cell hardware from Scribner Associates Inc. The anode employed an SGL 22BB gas diffusion layer (GDL) with a 6 mil oversized fluorinated ethylene propylene (FEP) gasket and a 0.5 mil active-area FEP gasket. The cathode used a nickel mesh current collector supported by main FEP gaskets of 20, 23, and 30 mil for the 0.5, 2.0, and 5.0 mgC/cm<sup>2</sup> interlayer loadings, respectively, to compensate for the added interlayer thickness. A 0.5 mil active-area FEP gasket was also added to the cathode side. A flow-through flow field was used

on the air side and a single-serpentine flow field on the anode. The cell assembly in the hardware was torqued uniformly to 120 in-lb using a calibrated torque wrench. Following assembly, the cell was connected to a Scribner 850e fuel cell test station for gas, temperature, and humidity control.

### ***Break-in procedure***

To activate the catalyst layers, the cell was heated to 40 °C and underwent a break-in procedure consisting of progressive current steps in 10 mA/cm<sup>2</sup> increments, each held for 5-10 mins, under 500 sccm H<sub>2</sub>/O<sub>2</sub> feed at 70% RH until the terminal cell voltage reached 0.2 V. This ensured proper membrane hydration and catalyst activation prior to subsequent testing.

### ***High-frequency resistance (HFR) and impedance measurements***

After activation, electrochemical impedance spectroscopy (EIS) was performed at 0 mA/cm<sup>2</sup> using a potentiostat (VMP2, BioLogic) to determine the high-frequency resistance (HFR) and assess the cell's ohmic characteristics.

### ***CO<sub>2</sub> capture experiments***

CO<sub>2</sub> capture performance was characterized by measuring the outlet CO<sub>2</sub> concentration from the cathode. The outlet gas was passed through a knockout drum equipped with a condenser and pump to remove condensate before entering a Teledyne TML20 CO<sub>2</sub> analyzer. The analyzer was calibrated prior to each experiment using CO<sub>2</sub>-free air for zero and a 400 ppm span mixture generated by blending 10% CO<sub>2</sub> (Keen Compressed Gas Co.) in air with CO<sub>2</sub>-free air. The total cathode and anode flowrate was 4000 sccm and 12.5 sccm, respectively. The anode was fed with pure hydrogen while the cathode was simulated air with 400 ppm CO<sub>2</sub>. Each set of operating conditions was maintained for 1 hour, during which data was collected at 10 s intervals. The reported values correspond to the average over the final 30 min.

### ***Membrane degradation: ion exchange***

It is known that the quaternary ammonium degrades in basic and dry environments.<sup>20</sup> Thus, controlled thermal membrane degradation was achieved by creating mixed counter ion exchange sites of HCO<sub>3</sub><sup>-</sup> and Cl<sup>-</sup>, where Cl<sup>-</sup> sites have higher thermal stability. Accordingly, the membrane was fully ion exchanged to HCO<sub>3</sub><sup>-</sup> form, followed by controlled partial Cl<sup>-</sup> ion exchange to produce defined hydroxide degradation fractions. Assuming all bicarbonate sites fully degrade, the required NaCl mass was calculated using the formula  $m_{\text{NaCl}}(\text{milligrams}) = 70.2 \cdot m_{\text{membrane}}(\text{grams}) \cdot \left(\frac{1}{d} - 1\right)$ , where  $d$  is the desired degradation fraction of cation sites. This calculation assumes that all the chloride will completely ion exchange with bicarbonate contained in the membrane due to the high relative affinity of chloride ions to PiperIon® membranes. The calculated amount of NaCl was dissolved in deionized (DI) water, and the membrane was soaked in this solution under stirring for 30 min. The membrane was then rinsed thrice in fresh DI water for 20 min each, wiped dry, and oven-dried at 120 °C for 24 h.

### ***Membrane degradation: ion exchange capacity (IEC) measurements***

The IEC was measured via a Potentiometric Titration protocol which has been outlined previously.<sup>21</sup> Membrane samples (~50 ± 10 mg) were immersed in 10 mL of an ion-exchange solution (4 mol NaCl/kg H<sub>2</sub>O + 0.02 mol KOH/kg H<sub>2</sub>O) for 20 min, followed by DI water rinsing. Conductivity of the rinse water was monitored and repeated until values of 3–4 μS/cm were achieved. Samples were then dried at 80 °C for 12 h, and the dry mass recorded. For titration, dried membranes were placed in 150 mL DI water with ~50 mg lithium triflate, and the solution was agitated for 30 min. A 2% v/v HNO<sub>3</sub> solution was prepared (1 mL in a 10 mL volumetric flask) and used for potentiometric titration with 0.02 M AgNO<sub>3</sub> using an automated titrator. The electrode was cleaned with Kimwipes before each run.

### ***Scanning electron microscopy (SEM)***

Cross-sectional imaging of the membranes was conducted using an Auriga 60 CrossBeam FIB/FE-SEM (Zeiss) operated at 1.5 kV. Samples were cryo-fractured in liquid nitrogen and sputter-coated with Au/Pd to improve surface conductivity.

## Theory

### Modeling objective

For our steady state, one-dimensional through-plane model of the anode, membrane, interlayer, and cathode (Fig. 1b), the ultimate objective is to calculate the electron efficiency,  $\eta_e = \frac{N_{CO_2}}{I/F}$ , where  $N_{CO_2}$  is the total carbon flux,  $I$  is the total current density, and  $F$  is Faraday's constant. By varying the physical parameters of the MEA, we aim to clarify how transport and reaction processes shape both the electron efficiency and the carbon flux. To achieve this, we must solve for several primitive variables, including the concentrations of hydroxide, bicarbonate, carbonate, the partial pressure of  $CO_2$ , the electronic potential, and the ionic potential. These variables serve as the foundation for the governing transport equations and kinetic models. As a global constraint, both the cell voltage and the total  $CO_2$  flux must remain positive throughout the system to yield a numerical solution. Consequently, model plots are truncated at high flux values, as this is where the cell voltage reaches zero. In-plane channel gradients, gas-phase pressure drops, and explicit water management coupling are neglected as the model is focused on capturing  $CO_2$  transport and reaction related limitations. All parameters used in the model are listed in the Appendix.

### Degree of freedom (DOF) analysis

The number of independent species balances is determined by<sup>22</sup>

$$N_{\text{species balances}} = N_{\text{species}} - N_{\text{specifications}} \quad [9]$$

$$N_{\text{specifications}} = 1 \text{ (electroneutrality)} + N_{\text{species relationships}} \quad [10]$$

Specifications include electroneutrality and chemical relationships, such as ionic equilibria between bicarbonate, carbonate, and hydroxide. For example, in the porous electrodes, there are four species and two specifications, and thus, there are two independent species balances. Similarly, there are two independent charge balances in these layers. Table II summarizes the primitive variables and number of independent species and charge balances for all four layers in the model.

### Independent conservation equations

To develop a numerical model, we focus on deriving the governing differential equations for a porous electrode (anode/cathode), which represents the most general model. By deriving the porous electrode model first, we establish the fundamental governing equations needed for all layers. The models for the membrane and interlayer are then obtained as reductions of the electrode model. Using the degree of freedom (DOF) analysis, we can define useful conservation equations for the porous electrode model. A carbon balance is written as

$$\nabla N_{CO_2} = \nabla N_{CO_2, \text{gas}} + \nabla N_C + \nabla N_B \quad [11]$$

$$N_{CO_2} = N_{CO_2, \text{gas}} + N_C + N_B \quad [12]$$

Where  $N_{CO_2, \text{gas}}$  is the gaseous  $CO_2$  flux,  $N_C$  is carbonate flux, and  $N_B$  is bicarbonate flux. At steady state, the total carbon flux must be a constant throughout the system and thus not depend on position. Additionally, a gaseous carbon dioxide species balance can be written based on the kinetic reactions from Eqs. 1-2

$$0 = \nabla N_{CO_2, \text{gas}} - (r_{OH^-} + r_{H_2O}) \quad [13]$$

Where  $r_{H_2O}$  and  $r_{OH^-}$  are the rate models for the water and hydroxide  $CO_2$  kinetic paths, respectively.

Similarly, a total charge balances is written as

$$0 = \nabla i_1 + \nabla i_2 \quad [14]$$

$$I = i_1 + i_2 \quad [15]$$

Where  $i_1, i_2$  are the electronic and ionic current densities, respectively. An ionic charge balance can relate the net consumption of ions to a Butler-Volmer expression,  $j_n$

$$\nabla i_2 = j_n \quad [16]$$

The additional specifications previously discussed include electroneutrality (Eq. 17) and equilibrium between the ionic species (Eq. 18). These specifications can be employed to express all ionic concentrations in terms of pH as follows

$$c_H + 2c_C + c_B = c_0 \quad [17]$$

$c_i$  represent concentration of species  $i$ , with  $i = C, H, B, o$  corresponding to carbonate, hydroxide, bicarbonate and total cation sites. Furthermore, because the ionic equilibrium constants are defined on a molality basis, the thermodynamic constant  $K_{b1}$  associated with Eq. 5 is used in a reparametrized form that incorporates the necessary conversion factors for concentration-based governing equations. Throughout the model derivation, similar reparameterization is applied to other physical parameters and is denoted with a '\*'.

$$K_{b1}^* = K_{b1} \phi_w \rho_w = \frac{c_H c_B}{c_C} \quad [18]$$

Here,  $\phi_w$  is the water volume fraction in the ionomer,  $\rho_w$  is the density of water. Combining equations Eqs. 17-18 with  $c_H = 10^{pH - pK_w}$ , all ionic concentrations can be expressed in terms of pH

$$c_H = 10^{pH - pK_w} \quad [19]$$

$$c_B = \frac{K_{b1}^* (c_0 - c_H)}{2c_H + K_{b1}^*} \quad [20]$$

$$c_C = \frac{c_H (c_0 - c_H)}{2c_H + K_{b1}^*} \quad [21]$$

which simplifies the numerical procedure. These conservation equations and specifications fully define the 1-D porous electrode model. Following this section, all gradients are expressed as derivatives along the x-direction.

### Governing equations

Based on the resulting conservation equations, we can now employ constitutive, transport, and kinetic relationships to formulate the full 1-D numerical porous-electrode model. The next step is to identify the most convenient set of unknowns to solve the model while maintaining modeling simplicity. In particular, we aim to keep all governing equations as 1<sup>st</sup> order ordinary differential equations (ODEs), since higher-order ODEs increase computational complexity, such as requiring additional boundary conditions. By rearranging Eq. 12 and applying Fick's Law of Diffusion and Bruggeman Relationship ( $N_{CO_2, gas} = \frac{D_{CO_2} \cdot \epsilon_g^3}{RT} \frac{dp_{CO_2}}{dx}$ ), we can solve for the CO<sub>2</sub> partial pressure gradient

$$\frac{dp_{CO_2}}{dx} = -(N_{CO_2} - N_{CB}) \frac{RT}{D_{CO_2} \cdot \epsilon_g^3} \quad [22]$$

where  $\epsilon_g$  is the volume fraction of void space,  $p_{CO_2}$  is the partial pressure of CO<sub>2</sub>,  $N_{CB} \equiv N_C + N_B$ ,  $D_{CO_2}$  is the bulk diffusion constant for CO<sub>2</sub>,  $R$  is the universal gas constant, and  $T$  is the temperature. The term  $N_{CB}$  appears because part of the total carbon flux is carried by dissolved ionic species rather than gas; grouping them simplifies the equations and reduces the number of unknowns. While Eq. 13 could be decomposed down to its primitive species ( $p_{CO_2}, c_C, c_B, \phi_2$ ), this would generate 2<sup>nd</sup> order ODEs in all of these terms, producing complexity for standard ODE solvers. Instead, 1<sup>st</sup> order ODEs can be conveniently maintained through the combination of Eq. 11 and Eq. 13, resulting in

$$\frac{dN_{CB}}{dx} = r_{OH^-} + r_{H_2O} = R_{CO_2} \quad [23]$$

Thus far,  $p_{CO_2}$  and  $N_{CB}$  are chosen as primary unknowns for solving the model, allowing us to preserve first-order ODEs. Via Eqs. 1-4, it can be shown that the overall rate equation ( $R_{CO_2}$ ) is

$$R_{CO_2} = \epsilon_{ion} (k_{1f}^* + k_{2f}^* c_H) \left( K_{CO_2}^* p_{CO_2} - K_{B2}^* \frac{c_B}{c_H} \right) = f(pH, p_{CO_2}) \quad [24]$$

Where  $k_{1f}^*$  and  $k_{2f}^*$  is the forward rate constant for  $r_1$  and  $r_2$ , respectively. The terms  $\epsilon_{\text{ion}}$ ,  $K_{\text{CO}_2}^*$ ,  $K_{\text{B}2}^*$  denote the ionomer volume fraction in the electrode, Henry's law constant for  $\text{CO}_2$ , and equilibrium constant for Equation 4.

Overall, Eq. 23 depends on the unknowns pH and  $p_{\text{CO}_2}$ . Since we have a differential equation for  $p_{\text{CO}_2}$  already, we must also develop a differential equation for pH. To do this, we apply Faraday's Law, the Nernst-Planck equation, the Bruggeman Relationship, and  $N_{\text{CB}}$  which are rewritten in terms of pH and  $\phi_2$

$$i_2 = \epsilon_{\text{ion}}^{1.5} F \left( D_{\text{H}} \frac{dc_{\text{H}}}{dp\text{H}} + 2D_{\text{C}} \frac{dc_{\text{C}}}{dp\text{H}} + D_{\text{B}} \frac{dc_{\text{B}}}{dp\text{H}} \right) \nabla p\text{H} - \frac{F^2 \epsilon_{\text{ion}}^{1.5}}{RT} (D_{\text{H}} c_{\text{H}} + 4D_{\text{C}} c_{\text{C}} + D_{\text{B}} c_{\text{B}}) \nabla \phi_2 \quad [25]$$

$$N_{\text{CB}} = -\epsilon_{\text{ion}}^{1.5} \left( D_{\text{C}} \frac{dc_{\text{C}}}{dp\text{H}} + D_{\text{B}} \frac{dc_{\text{B}}}{dp\text{H}} \right) \nabla p\text{H} + \frac{F \epsilon_{\text{ion}}^{1.5}}{RT} (2D_{\text{C}} c_{\text{C}} + D_{\text{B}} c_{\text{B}}) \nabla \phi_2 \quad [26]$$

where  $\epsilon_{\text{ion}}$  is the volume fraction of ionomer,  $F$  is Faraday's constant,  $D_i$  represents the diffusion coefficient for species  $i$ ,  $\phi_2$  is the ionic potential, and chain rule derivatives,  $\frac{dc_i}{dp\text{H}}$ , relate the species concentrations to pH. By rearranging Eqs. 25-26 into matrix form, Eqs. 27-28 provide explicit expressions for the spatial gradients of pH and the ionic potential

$$\frac{dp\text{H}}{dx} = \frac{-dd \cdot i_2 - bb \cdot N_{\text{CB}}}{aa \cdot dd - bb \cdot cc} \quad [27]$$

$$\frac{d\phi_2}{dx} = \frac{cc \cdot i_2 - aa \cdot N_{\text{CB}}}{aa \cdot dd - bb \cdot cc} \quad [28]$$

where the coefficients  $aa$ ,  $bb$ ,  $cc$ , and  $dd$  are grouping terms introduced to simplify notation and are defined by the following matrix

$$\begin{bmatrix} aa & bb \\ cc & dd \end{bmatrix} = \begin{bmatrix} F \epsilon_{\text{ion}}^{1.5} \left( D_{\text{H}} \frac{dc_{\text{H}}}{dp\text{H}} + 2D_{\text{C}} \frac{dc_{\text{C}}}{dp\text{H}} + D_{\text{B}} \frac{dc_{\text{B}}}{dp\text{H}} \right) - \frac{F^2 \epsilon_{\text{ion}}^{1.5}}{RT} (D_{\text{H}} c_{\text{H}} + 4D_{\text{C}} c_{\text{C}} + D_{\text{B}} c_{\text{B}}) & \\ -\epsilon_{\text{ion}}^{1.5} \left( D_{\text{C}} \frac{dc_{\text{C}}}{dp\text{H}} + D_{\text{B}} \frac{dc_{\text{B}}}{dp\text{H}} \right) & \frac{F \epsilon_{\text{ion}}^{1.5}}{RT} (2D_{\text{C}} c_{\text{C}} + D_{\text{B}} c_{\text{B}}) \end{bmatrix}$$

In summary, we now have expressions for the spatial gradients of  $p_{\text{CO}_2}$ ,  $N_{\text{CB}}$ , pH, and  $\phi_2$ ; however, Eq. 28 depends on the ionic current density. To maintain 1<sup>st</sup> order ODEs,  $i_2$  can be treated as an unknown. Equation 16 provides a differential equation for  $i_2$ , which, when combined with the Butler-Volmer kinetic expression, yields the following expression

$$\frac{di_2}{dx} = j_n = j_{v,o} \left( \exp\left(\frac{\alpha_a F \eta_s}{RT}\right) - \exp\left(\frac{-\alpha_c F \eta_s}{RT}\right) \right) \quad [29]$$

where  $j_{v,o}$  is the exchange current density,  $\alpha_a$  and  $\alpha_c$  are the anodic and cathodic transfer coefficients. For proton-based redox reactions, the surface overpotential, accounting only for pH differences, is defined as

$$\eta_s = \phi_1 - \phi_2 - \left( E_o - \frac{RT}{F} \text{Ln}(10) \text{pH} \right) \quad [30]$$

$E_o$  is a standard potential and  $\phi_1$  is the electronic potential. Finally, Eq. 29 depends on  $\phi_1$  which can be derived simply from Eq. 15 and Ohm's Law as

$$\frac{d\phi_1}{dx} = \frac{I - i_2}{\sigma} \quad [31]$$

employing an electronic conductivity term,  $\sigma$ . Overall, the electrode model can be completely solved through the set of selected unknowns ( $p_{\text{CO}_2}$ ,  $N_{\text{CB}}$ , pH,  $i_2$ ,  $\phi_2$ ,  $\phi_1$ ). As discussed in the Appendix, the membrane ( $\phi_2$ , pH) and interlayer ( $p_{\text{CO}_2}$ ,  $N_{\text{CB}}$ , pH,  $\phi_2$ ) involve fewer unknowns because they lack electrochemical kinetics and, for the membrane, contain only ionic transport. Details of the boundary conditions for all layers are presented in the appendix.

## Results and Discussion

### Model validation and baseline diagnostic of HEMCC

To guide experiments toward higher electron efficiency, we first validated our baseline experiments using a one-dimensional electrochemical model as measured by the electron efficiency-CO<sub>2</sub> flux and current-voltage relationships. Figure 2a shows that the model closely matches experimental electron efficiency across all flux values, with a peak efficiency occurring around 300 kgCO<sub>2</sub>/m<sup>2</sup>/yr. Similarly, Fig. 2b demonstrates good agreement between modeled and experimental cell voltage as a function of current density, confirming the model captures key electrochemical behavior.

Although current density is the controlled variable, we plot electron efficiency versus CO<sub>2</sub> flux because both are key performance metrics for DAC costs, whereas current density alone is not. This is because CO<sub>2</sub> flux, and current density are related through  $N_{\text{CO}_2} = I \frac{\eta_e}{F}$ . Importantly, throughout this report, higher CO<sub>2</sub> flux can also be interpreted as a higher rate of hydroxide generation, providing context for transport and reaction behavior.

To identify the dominant losses of electron efficiency, we developed an efficiency loss diagram by performing a steady state analysis of the membrane through a carbon balance, and Faraday's Law expressed as:

$$\eta_e = 1 - \frac{N_C + N_H}{2N_C + N_H + N_B} \quad [32]$$

To analyze the contributions of each ionic species to electron efficiency, we decompose  $\eta_e$  into its diffusion and migration components for carbonate and hydroxide

$$\begin{aligned} \eta_e &= 1 - \frac{\frac{F}{RT} (2D_C c_C + D_H c_H) \nabla \Phi_2 - (D_C \nabla c_C + D_H \nabla c_H)}{\frac{F}{RT} (4D_C c_C + D_H c_H + D_B c_B) \nabla \Phi_2 - (2D_C \nabla c_C + D_H \nabla c_H + D_B \nabla c_B)} \\ &= 1 - \eta_{e,\text{CO}_3^{2-}}^M - \eta_{e,\text{CO}_3^{2-}}^D - \eta_{e,\text{OH}^-}^M - \eta_{e,\text{OH}^-}^D \end{aligned} \quad [33]$$

Here,  $R$  is the universal gas constant,  $T$  is the temperature.  $D_i$  and  $c_i$  represent the diffusion coefficient and concentration of species  $i$ , with  $i = C, H, B$ , corresponding to carbonate, hydroxide, and bicarbonate. The term  $\nabla c_i$  denotes the concentration gradients, and  $\nabla \Phi_2$  is the ionic potential gradient.  $\eta_{n,m}$  is the a loss contribution to electron efficiency, where  $n$  is migration or diffusion, and  $m$  is carbonate or hydroxide. In this expanded form, the numerator represents the combined diffusion and migration flux of carbonate and hydroxide ions, while the denominator represents the total charge flux, which also includes bicarbonate. Electron efficiency approaches its theoretical maximum, unity, as carbonate and hydroxide fluxes go to zero; this maximum electron efficiency corresponds to pure bicarbonate transport. To further quantify the contributions of each species to charge transport, we define the current fraction for each species as  $z_i N_i / I$ , where  $z_i$  is the charge number of ionic species  $i$ . Both the electron efficiency components and the current fraction contributions are normalized by the total current and averaged over the membrane length, providing a single representative value for a given CO<sub>2</sub> flux.

The current fraction diagram (Fig. 2d) reveals the proportions of net charge transport from cathode to anode for bicarbonate, carbonate, and hydroxide. At low to medium flux values, both carbonate and bicarbonate contribute significantly to charge transport. Since the migration component of bicarbonate must be positive, this negative flux is caused by bicarbonate back-diffusion. At higher flux values, hydroxide transport loss becomes more prominent. This is because hydroxide at the cathode/interlayer has two competing outcomes: it can either leak through the membrane without reacting (transport pathway) or react with CO<sub>2</sub> (capture pathway). The presence of hydroxide in the membrane indicates that the capture pathway is slower than the transport pathway.

To guide improvements in electron efficiency, the efficiency loss diagram (Fig. 2c) provides a breakdown of the relative contributions of each loss component. At low flux values (<200 kgCO<sub>2</sub>/m<sup>2</sup>/yr), carbonate diffusion dominates. Generally, higher membrane resistance will reduce diffusion relative to migration due to a larger ohmic potential drop. Thus, carbonate diffusion losses may be mitigated by increasing membrane resistance, either by reducing ionic conductivity or increasing membrane thickness. At higher flux values (>500 kgCO<sub>2</sub>/m<sup>2</sup>/yr), hydroxide transport emerges as the largest contributor to loss. Here, the productive OH<sup>-</sup> capture pathway could be enhanced by increasing the interlayer thickness, which extends the reaction path for hydroxide and CO<sub>2</sub>. Alternatively, increasing cathode thickness could improve CO<sub>2</sub> capture, but it is less cost-effective due to catalyst loading.

Overall, these observations from the efficiency loss diagram provide a conceptual basis for exploring targeted performance-improving strategies. Thus, we will test two key hypotheses through modeling and experiments aimed at improving electron efficiency relative to the baseline:

- (i) For low flux values, increasing membrane resistance will improve electron efficiency by reducing carbonate diffusion losses
- (ii) For high flux values, increasing interlayer thickness will improve electron efficiency by mitigating hydroxide losses

### ***Membrane resistance effects: model predictions, experimental validation, and mechanistic analysis***

We used our model to test the hypothesis that increasing membrane resistance can improve electron efficiency at low flux values (Fig. 3a). By systematically reducing membrane conductivity by factors of 1, 10, and 100 relative to the baseline, the model predicts that higher membrane resistance raises the peak electron efficiency and shifts the optimum to lower CO<sub>2</sub> flux, while maintaining a similar efficiency–flux shape. These results indicate that electron efficiency improvements at low flux are a direct consequence of increased membrane resistance, supporting the hypothesized mechanism.

To experimentally verify the effect of membrane resistance, we performed progressive degradation of quaternary ammonium sites of the polymer through controlled thermal degradation (Fig. 3b). Through measurements of IEC, we confirm that the quaternary ammonium exchange sites were degraded (see methods). Additionally, we confirmed the increase in membrane resistance for the 0, 30, and 45% degraded membranes through HFR<sub>OH<sup>-</sup></sub> values at 0 mA/cm<sup>2</sup>, which were 1.0, 3.2, and 4.9 Ohm-cm<sup>2</sup>. Thermally degraded membranes also exhibited a visible color change, shifting from transparent to a yellowish color (Fig. 3c). A possible explanation of this observation is that degradation of quaternary ammonium groups produces tertiary amine sites.<sup>23</sup> Furthermore, the color change may be due to N-O bond formation resulting from oxidation of these tertiary amine sites, providing additional evidence for successful quaternary ammonium site degradation. However, further confirmation of this mechanism is beyond the scope of this study.

Importantly, the experimental trends align well with the model predictions (Fig. 3a), showing that increasing membrane resistance primarily improves electron efficiency at low flux values. This is consistent with the concept that membrane resistance primarily mitigates carbonate diffusion losses, which are most significant at low flux values, as shown in Fig. 2c. The next section will focus on determining the mechanistic effect of higher membrane resistance on ion transport.

While membrane resistance improves electron efficiency, it is localized to low flux values due to a reduction in carbonate diffusion losses. Overall, a more resistive membrane increases electron efficiency primarily by reducing carbonate diffusion losses. However, this improvement comes at the cost of increased migration losses. Figure 4d demonstrates that the dominant transport mechanism shifts from diffusion to migration. Comparing Fig. 2c and 4a reveals a significant reduction in the carbonate diffusion region, accompanied by an increase in the migration regions of both carbonate and hydroxide. Furthermore, the dimensionless concentration profiles at a fixed flux value indicate that higher membrane resistance shifts the ionic equilibrium toward carbonate species. The ionic potential profiles confirm that a more resistive membrane increases the migration driving force, leading to increased migration.

As shown by the current fraction changes, increasing membrane resistance reduces bicarbonate transport but increases hydroxide transport. At higher flux values, hydroxide migration becomes more dominant (Figs. 4b-c). This is because the migration rate of hydroxide increases relative to the unchanged capture rate, as described previously. The result of this hydroxide consumption mismatch is hydroxide leakage through the membrane. To address this, a thick interlayer can provide a dual benefit: it increases ion transport resistance to reduce carbonate diffusion losses and provides more reaction volume for hydroxide to react with carbon dioxide, thereby reducing hydroxide leakage through the membrane. These effects can help enhance carbon dioxide capture to promote higher electron efficiency at low and high fluxes.

### ***Interlayer thickness effects: model predictions, experimental validation, and mechanistic analysis***

We hypothesized that a thicker interlayer would improve performance, particularly at high CO<sub>2</sub> flux values, and confirmed this experimentally by increasing the interlayer loading (Fig. 5a). In the model, increasing the interlayer thickness from 23, 92, and 230 μm resulted in progressively higher electron efficiencies across all flux values, as



























$$\Delta f_{CO_2} = \sqrt{\left(\frac{x_{CO_2,out}^{Ca} V_{out}^{Ca} + x_{CO_2,out}^{An} V_{out}^{An}}{x_{CO_2,in}^{Ca} V_{in}^{Ca}} \Delta(x_{CO_2,in}^{Ca} V_{in}^{Ca})\right)^2 + \left(\frac{\Delta(x_{CO_2,out}^{Ca} V_{out}^{Ca})}{x_{CO_2,in}^{Ca} V_{in}^{Ca}}\right)^2 + \left(\frac{\Delta(x_{CO_2,out}^{An} V_{out}^{An})}{x_{CO_2,in}^{Ca} V_{in}^{Ca}}\right)^2} \quad [A. 8]$$

where the uncertainty of each CO<sub>2</sub> flow term is calculated using standard propagation for a product of independent variables  $\Delta(x_{CO_2,in}^{Ca} V_{in}^{Ca}) = x_{CO_2,in}^{Ca} V_{in}^{Ca} \cdot \sqrt{\left(\frac{\Delta x_{CO_2,in}^{Ca}}{x_{CO_2,in}^{Ca}}\right)^2 + \left(\frac{\Delta V_{in}^{Ca}}{V_{in}^{Ca}}\right)^2}$ . The same approach is applied to  $\Delta(x_{CO_2,out}^{Ca} V_{out}^{Ca})$  and  $\Delta(x_{CO_2,out}^{An} V_{out}^{An})$ .

The reported CO<sub>2</sub> flux reported is calculated as

$$\text{Flux} = \frac{x_{CO_2,in}^{Ca} V_{in}^{Ca} - x_{CO_2,out}^{Ca} V_{out}^{Ca}}{V_{IG} A_{cell}} \quad [A. 9]$$

### References

- 1 IPCC, 2023: *Climate Change 2023: Synthesis Report. Contribution of Working Groups I, II and III to the Sixth Assessment Report of the Intergovernmental Panel on Climate Change*. IPCC, Geneva, Switzerland., Intergovernmental Panel on Climate Change (IPCC), First., 2023.
- 2 *Net Zero by 2050 - A Roadmap for the Global Energy Sector*.
- 3 R. Rohde, Global Temperature Report for 2024, <https://berkeleyearth.org/global-temperature-report-for-2024/>, (accessed 13 November 2025).
- 4 *Decarbonising hard-to-abate sectors with renewables: Perspectives for the G7*.
- 5 O. Y. Edelenbosch, A. F. Hof, M. van den Berg, H. S. de Boer, H.-H. Chen, V. Daioglou, M. M. Dekker, J. C. Doelman, M. G. J. den Elzen, M. Harmsen, S. Mikropoulos, M. A. E. van Sluisveld, E. Stehfest, I. S. Tagomori, W.-J. van Zeist and D. P. van Vuuren, *Nat. Clim. Chang.*, 2024, **14**, 715–722.
- 6 International Energy Agency, *Direct Air Capture: A key technology for net zero*, OECD, 2022.
- 7 N. McQueen, K. V. Gomes, C. McCormick, K. Blumanthal, M. Pisciotta and J. Wilcox, *Prog. Energy*, 2021, **3**, 032001.
- 8 L. Shi, Y. Zhao, S. Matz, S. Gottesfeld, B. P. Setzler and Y. Yan, *Nat Energy*, 2022, **7**, 238–247.
- 9 S. Matz, B. P. Setzler, C. M. Weiss, L. Shi, S. Gottesfeld and Y. Yan, *J. Electrochem. Soc.*, 2021, **168**, 014501.
- 10 W. A. Rigdon, T. J. Omasta, C. Lewis, M. A. Hickner, J. R. Varcoe, J. N. Renner, K. E. Ayers and W. E. Mustain, *Journal of Electrochemical Energy Conversion and Storage*, 2017, **14**, 020701.
- 11 A. P. Muroyama, A. Beard, B. Pribyl-Kranewitter and L. Gubler, *ACS EST Eng.*, 2021, **1**, 905–916.
- 12 H. Seo and T. A. Hatton, *Nat Commun*, 2023, **14**, 313.
- 13 P. Zhu, Z.-Y. Wu, A. Elgazzar, C. Dong, T.-U. Wi, F.-Y. Chen, Y. Xia, Y. Feng, M. Shakouri, J. Y. (Timothy) Kim, Z. Fang, T. A. Hatton and H. Wang, *Nature*, 2023, **618**, 959–966.
- 14 Z. Siroma, S. Watanabe, K. Yasuda, K. Fukuta and H. Yanagi, *ECS Trans.*, 2010, **33**, 1935.
- 15 K. N. Grew, X. Ren and D. Chu, *ECS Trans.*, 2011, **41**, 1979.
- 16 H.-S. Shiau, I. V. Zenyuk and A. Z. Weber, *J. Electrochem. Soc.*, 2017, **164**, E3583.
- 17 J. A. Wrubel, A. A. Peracchio, B. N. Cassenti, T. D. Myles, K. N. Grew and W. K. S. Chiu, *ECS Trans.*, 2017, **80**, 989.
- 18 U. Krewer, C. Weinzierl, N. Ziv and D. R. Dekel, *Electrochimica Acta*, 2018, **263**, 433–446.
- 19 M. R. Gerhardt, L. M. Pant and A. Z. Weber, *J. Electrochem. Soc.*, 2019, **166**, F3180.
- 20 D. R. Dekel, M. Amar, S. Willdorf, M. Kosa, S. Dhara and C. E. Diesendruck, *Chem. Mater.*, 2017, **29**, 4425–4431.
- 21 L. Wang, S. Rojas-Carbonell, K. Hu, B. P. Setzler, A. R. Motz, M. E. Ueckermann and Y. Yan, *Front. Energy Res.*, DOI:10.3389/fenrg.2022.887893.
- 22 T. F. Fuller and J. N. Harb, *Electrochemical Engineering*, John Wiley & Sons, 2018.
- 23 W. E. Mustain, M. Chatenet, M. Page and Y. S. Kim, *Energy Environ. Sci.*, 2020, **13**, 2805–2838.
- 24 B. Corry, *Nature Chem.*, 2018, **10**, 799–800.
- 25 E. R. Jr. Nightingale, *J. Phys. Chem.*, 1959, **63**, 1381–1387.
- 26 A. M. Kiss, T. D. Myles, K. N. Grew, A. A. Peracchio, G. J. Nelson and W. K. S. Chiu, *J. Electrochem. Soc.*, 2013, **160**, F994–F999.
- 27 M.-L. Liu, Y. Chen, C. Hu, C.-X. Zhang, Z.-J. Fu, Z. Xu, Y. M. Lee and S.-P. Sun, *Nat Commun*, 2024, **15**, 7271.

- 1  
2  
3 28 C. Lu, C. Hu, Z. Chen, P. Wang, F. Feng, G. He, F. Wang, Y. Zhang, J. Z. Liu, X. Zhang and J. Qu, *Science*  
4 *Advances*, 2023, **9**, eadf8412.  
5 29 A. Wang, C. Breakwell, F. Foglia, R. Tan, L. Lovell, X. Wei, T. Wong, N. Meng, H. Li, A. Seel, M. Sarter, K.  
6 Smith, A. Alvarez-Fernandez, M. Furedi, S. Guldin, M. M. Britton, N. B. McKeown, K. E. Jelfs and Q. Song,  
7 *Nature*, 2024, **635**, 353–358.  
8 30 Hydrogen Shot, <https://www.energy.gov/eere/fuelcells/articles/hydrogen-shot-introduction>, (accessed 17  
9 November 2025).  
10 31 T. R. Marrero and E. A. Mason, *Journal of Physical and Chemical Reference Data*, 1972, **1**, 3–118.  
11 32 A. L. Buck, .  
12 33 X. Luo, S. Rojas-Carbonell, Y. Yan and A. Kusoglu, *Journal of Membrane Science*, 2020, **598**, 117680.  
13 34 J. J. Carroll, J. D. Slupsky and A. E. Mather, *J. Phys. Chem. Ref. Data*, 1991, **20**, 1201–1209.  
14 35 F. Milljzro, .  
15 36 A. Stefánsson, P. Bénézech and J. Schott, *Geochimica et Cosmochimica Acta*, 2013, **120**, 600–611.  
16 37 X. Wang, W. Conway, R. Burns, N. McCann and M. Maeder, *J. Phys. Chem. A*, 2010, **114**, 1734–1740.  
17 38 W. Sheng, H. A. Gasteiger and Y. Shao-Horn, *J. Electrochem. Soc.*, 2010, **157**, B1529.  
18 39 J. Suntivich, H. A. Gasteiger, N. Yabuuchi and Y. Shao-Horn, *J. Electrochem. Soc.*, 2010, **157**, B1263.  
19 40 J. Wang, Y. Zhao, B. P. Setzler, S. Rojas-Carbonell, C. Ben Yehuda, A. Amel, M. Page, L. Wang, K. Hu, L. Shi,  
20 S. Gottesfeld, B. Xu and Y. Yan, *Nat Energy*, 2019, **4**, 392–398.  
21  
22  
23  
24  
25  
26  
27  
28  
29  
30  
31  
32  
33  
34  
35  
36  
37  
38  
39  
40  
41  
42  
43  
44  
45  
46  
47  
48  
49  
50  
51  
52  
53  
54  
55  
56  
57  
58  
59  
60